capstract:2611.00010v1 [stat.AP] 5 Nov 2026

Agreement of independently calibrated equivalent counts across measurement systems

Daria E. Veldran[1,*] Luís M. Taveiro[2] Eun-seo Ryun[3,1] Amal Z. Redhani[4]
[1]Division of Statistical Metrology, Marven Institute, Rotterdam, Netherlands
[2]Centre for Environmental Measurements, Instituto do Vale Cerdeiro, Aveiro, Portugal
[3]Department of Planetary Radiometry, Saeum Institute of Science, Daejeon, Republic of Korea
[4]Department of Administrative Records, El Manarif School of Public Studies, Tunis, Tunisia

November 5, 2026

Abstract

We compare equivalent counts obtained by independently calibrating local unit responses in seven measurement systems. The measurements range from static displacement to time-integrated radiative flux and require additive, multiplicative and mixture corrections. We derive a uniqueness result for equivalent counts on a calibrated composition law and apply it prior to pooling. Six discovery systems give a common estimate of 42.02 (standard uncertainty 0.08). The estimate predicts a net release of 57.96 kJ per square meter during a held-out interval of lunar totality, with a recovered release of 58.02 kJ per square meter. Simultaneous uncertainty intervals admit a single integer in each system. The correspondence applies to the specified measurement boundaries and can be tested in systems for which the unit response is available separately from the full measurement.

Keywords: equivalent count, measurement uncertainty, dimensional analysis, radiative balance

1 Introduction

A count can be estimated without identifying its constituents. An optical depth is sometimes stated in units of a reference column. A specimen that supplies six times the water retained by a reference wafer can be reported as six wafer equivalents even if it was never cut. Both statements depend on the response of a part that can be measured by itself. The response of the whole may be of little use until the part has been specified.

This distinction supplements dimensional analysis [4, 5]. For example, dividing the travel of a drawer by its full width gives a dimensionless result with a clear geometric interpretation. Dividing the same travel by the shift produced by one index of its depth stop gives a quantity that predicts the effect of a second index. The numerator does not distinguish these two ratios. The way the denominator is obtained does.

∗Corresponding author: d.veldran@marven.example

A comparison of two such ratios arose during an exchange of apparatus between the Marven and Cerdeiro laboratories [8]. The two values differed by about one tenth of an index, although the measurements involved a runner and a sheet of dried bread. The difference was smaller than the manufacturing tolerances on either specimen. The next measurements used the energy of a cistern impulse response and the empty-cell fraction of a pollen collector.

The present analysis starts with the actual observation law in each system. It then asks whether a single dimensionless value can replace the specimen parameter in that law. The six discovery cases include an archive in which the subject of measurement disappears at publication and a sediment core for which only its exterior is accessible. The seventh observation was kept sealed until the six-system estimate and its rule for integer prediction had been deposited. Its local standard was available throughout.

2 Calibrated composition

Let r denote a repeatable response, e its neutral value and a the response of a unit standard. In a series experiment a second standard may add to the first response, or it may act on the response already present. Stevens's distinction between admissible scale transformations and empirical operations is relevant here [21]. Changing volts to millivolts and changing a parallel contact to a series contact have quite different consequences for a count.

Some instruments have an observation map M whose argument is the composable response. For a fixed acquisition protocol we use the coordinate

$$N(y) = \frac{g(M^{-1}(y))}{g(a)}, \qquad g(r \circ s) = g(r) + g(s), \qquad g(e) = 0. \tag{1}$$

The symbol M^{-1} denotes recovery of the identified scalar response, after reduction over nuisance parameters. Several records may be needed to obtain one y. For a balance, M is a subtraction of the blank and the natural g is the identity. For an energy fraction, M can include the receiver offset and $g = -\log$ converts successive fractional losses to additive decrements. Mixture averaging is part of M. Taking a logarithm before or after recovering a mixture component can give substantially different counts.

Proposition 1 (Uniqueness of the calibrated count)**.** *Suppose the recoverable responses at fixed conditions form an interval I, with continuous composition $\circ$ and identity e. Suppose there is a continuous strictly monotone $g : I \to [0, \infty)$ onto this half line that takes composition to addition. For a specified standard $a \neq e$, any continuous count C with $C(a) = 1$ and $C(r \circ s) = C(r) + C(s)$ agrees with Eq. (1) on I.*

Proof. Write $F(t) = C(g^{-1}(t g(a)))$ for $t \geq 0$. The hypotheses give $F(s + t) = F(s) + F(t)$ and $F(1) = 1$. Repetition gives $F(m) = m$ on the nonnegative integers. Subdivision gives $qF(p/q) = p$ on the nonnegative rationals. Continuity then gives $F(t) = t$ on the half line. Substitution of $t = g(r)/g(a)$ proves the claim. ∎

This is the continuous additive functional equation [1]. We check the composition only over the calibrated range. Saturation of the instrument may destroy identifiability in y while leaving the statement about r intact.

The unit a is external to Proposition 1. Using a stack of two certified slices for a would halve the reported count. The stack is admissible for a repetition check and each of its two slices still counts separately. In the protocols below the unit was either specified by the apparatus or chosen

as the smallest body or transaction for which the calibration service already issued a result. The fit weights depend on measurement uncertainty. The unit selection precedes estimation of the specimen response.

3 Discovery measurements

For each system Table 1 gives the observation used in the final scalar inversion. Several rows give derived instrument readings, such as a low-frequency admittance after removal of the electrode contribution. The entries in the fourth column are the single-unit calibration, with its own sampling record. All counts are evaluated before rounding. Details sufficient to recover the entries from the displayed inputs are collected in Appendix A.

Table 1: Discovery readings and the subsequently unsealed radiometric reading. Each u is a standard uncertainty in count units. The final row was withheld from the six-system estimate.

System	Independent blocks	Observation	Unit response	N	u
Drawer runner	24	525.75 mm	12.500 mm	42.06	0.146
Crispbread sheet	20	6.2925 g	0.15000 g	41.95	0.186
Cistern decay	32	0.375370	0.977000	42.11	0.206
Marsh pollen	40	0.161261	0.02000	41.86	0.240
Minutes archive	64	36.25296 marks	0.56200 marks	42.08	0.217
Riverbed core	16	0.0889653 S/m²	0.25000 Ω m²	41.93	0.273
Lunar totality	1	58.0152 kJ/m²	1.3800 kJ/m²	42.04	0.320

3.1 Travel under load

The runner came from a cabinet with its stop removed. We measured the distance between the position at which the front face was flush and the position at which the rear pair of rollers first lost contact. This second position was marked by the change in slope of vertical deflection with applied load. Measuring to the end of the metal would have included an overhang during which the drawer was supported on one pair of rollers. The stopping surface was read on the outward traverse only. Reverse traverses gave a separate estimate of compliance.

The local standard was the displacement of the depth stop on a separate runner for one change of index with the same test load. Because the adjustment holes on this standard lie behind the faceplate, the operator measuring travel could neither count the holes nor see an index reading. Three carriages per block were used in the calibration. Translation of two successive indexes agreed with twice the one-index displacement within 0.05 mm after adjustment of the lead-screw datum [20]. The reported travel is 525.75 mm, which gives 42.06 indexes. The original service datum at the back flange would give 42.8 indexes.

3.2 Residual water in a baked sheet

In the bakery experiment we measure water left behind after a fixed drainage interval, at constant water activity and temperature. Capillary imbibition can give a square-root dependence on time at early contact [25]. Drainage and residual retention are separate operations. We used the mass at 90 s after withdrawal, when the empty wire support gave a flat trace in each run. The

standard is a separately baked calibration wafer of the same dough, prepared on the plant's quality-control die [12]. The assay uses its measured water uptake, 0.15000 g, including the residual surface film. The unit is one wafer, irrespective of the area cut by any particular production score.

The sheet was immersed intact. Scale drift was estimated by bracketing each sheet tare with two suspended references. A different sheet from the same batch was broken into four pieces and drained with the same exposed area to check the size of the edge contribution. New edges contributed to the balance at early times. By 90 s the difference between intact and partitioned sheets was 0.018 g on average after the blank correction. A simple correction based on perimeter increased the equivalent count by 0.12. The uncut specimen was used for the estimate because the reference wafer was also uncut. The null intercept of the response against the number of non-contacting reference wafers was within the blank repeatability.

3.3 Energy remaining in a cistern

The cistern was empty and dry. A loudspeaker and a receiving microphone exchanged positions between runs to reduce the effect of one dominant corner. The integrated impulse response, in the sense of Schroeder [19], was taken in the octave band centered at 1 kHz. We computed the ratio of the residual reflected energies at a separation of 0.840 s, with the start after direct arrival and the end before the noise floor. Sabine's diffuse-field approximation motivates composition of loss fractions [18]. The cistern still had detectable modes, so each energy curve was averaged over source and receiver pairs before the endpoint ratio was taken.

The calibration fixture used a dry coupon of the cistern lining. Its reflected hemisphere retained an energy fraction of 0.977000 under diffuse-incidence weighting. Repeated encounters with a rough return screen in the fixture gave the expected product after removal of the return screen's loss [3]. Under this convention the observed fraction P gives

$$N_{\mathrm{cis}} = \frac{-\log P}{-\log a}, \qquad a = 0.977000. \tag{2}$$

A count of impulse peaks depends on the detection threshold. We use the endpoint decrement in Figure 1, leaving the intermediate samples available to check the constant-loss approximation. Replacing the endpoint decrement with a least-squares slope over all plotted bins reduces the equivalent count by 0.19.

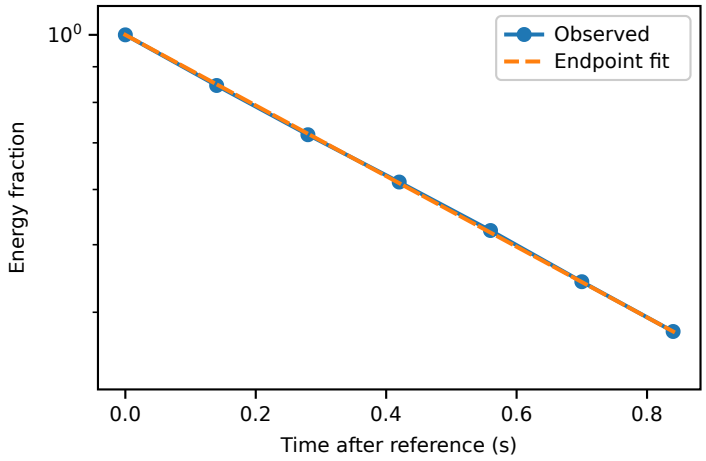


Figure 1: Cistern energy remaining after the reference time, divided by energy at the reference time. Points are ensemble means. The dashed curve is the constant fractional loss inferred from the endpoints.

3.4 Negative detections over a salt marsh

A marsh collector gives a set of empty or occupied cells. We used the empty fraction for a single taxon, after removing the estimated background, because a large grain deposit can make individual grains difficult to distinguish. Detection and occurrence enter the likelihood separately, as in repeated survey models [13, 17]. Reference flowering stems in a screened bed gave a mean intensity $\theta = 0.02000$ per stem in a single gate. The open collector integrated three equal gates under the same wind exposure.

Wind was common to the cells exposed at a given time. Conditional on normalized exposure W, the empty probability with N stem equivalents is $\exp(-3\theta W N)$. A gamma distribution for W with shape k and rate k fits the exposure-tracer observations [10, 23]. We fixed the shape at the tracer estimate $k = 3.00$ for the central calculation and propagated its uncertainty. Substituting the gamma Laplace transform gives

$$P_0 = (1 + 3\theta N / k)^{-k}, \qquad N_{\mathrm{marsh}} = \frac{k(P_0^{-1/k} - 1)}{3\theta}. \tag{3}$$

The corrected empty fraction is 0.161261, giving 41.86 equivalents. The three gates make up one observation. Treating them as separate realizations of W would change the inference. Fixing exposure at its mean gives $-\log(P_0)/0.06000 = 30.41$, a difference of 11.45 equivalents even at infinite sample size.

For one check we fitted the first two tracer moments separately by opening two short windows before and after the main collector gate. This yielded a somewhat narrower mixing distribution and a count lower by 0.12. The time series showed that the change was mostly attributable to one block in the lee of the access platform. We kept that block in both fits. Its packet of blank cells had been recorded before the tracer was processed.

3.5 Citations to annexes in published minutes

A publication office supplied sequential snapshots of council minute packets, including a copy of the artifact at public release. Its working amendments could be counted exactly for tracer packets

only. The archive retained compiled minutes and the marks that pointed to annexes. Several lines could enter the working packet as one filing and later produce a single mark or no mark. There were also marks inherited from the previous version. A mark counts each time it appears on a separate agenda line, even when the same annex is cited at two locations. We retained this definition in the tracer experiment to avoid an artificial ceiling on aggregate marks.

We used a source separation based on independent tracer amendments with synthetic annex labels. If B is the number of eligible inherited marks, X the number of visible marks from one amendment, and Y the total visible marks, then the working composition for a packet with m additions is

$$G_{Y\mid B,m}(z) = (1 - r + rz)^{B} G_{X}(z)^{m}, \qquad N_{\mathrm{arc}} = \frac{\overline{Y} - r\overline{B}}{G_{X}'(1)}. \tag{4}$$

Here G is a probability generating function and r is the marginal probability of retaining an eligible old mark. The first moment in Eq. (4) only requires marginal additivity. Correlation from a clerk deleting a group of lines together changes the variance. We fitted that variance at the deliberation block level. Records for different meetings of a standing committee were combined when the release office used the same compilation batch. The dependence of variance on packet size in such a compound count is familiar from random-sum models [7].

Release operators saw the synthetic labels in the same typographic style as other annex pointers. They could identify them as tracer marks only after the print audit [16]. Each tracer succeeded through a drafting gate with probability 0.80. The mean count of visible marks per success was 0.7025. Multiplication of the two estimates gives $G_{X}'(1) = 0.56200$. In the same tracer batches, $r = 0.4600$ for carried marks. The mean weighted inherited count was 27.4000, and the weighted released count was 36.25296 marks. The weights standardize short and long docket classes to the tracer mix. The derived count of amendments is 42.08 per packet at that mix. Dividing all printed marks by the calibrated yield would instead give 64.51. In particular, carrying more marks forward cannot by itself increase the estimate of the number introduced.

An increase in the gross response can arise entirely from carryover. In Eq. (4), a mean increase of one inherited mark raises the expected released count by 0.46 marks and has zero effect on the inferred additions.

3.6 Resistance of layered sediment

The core measurement uses a cylinder from freshwater riverbed sediment. Vertical conduction puts most of the fine material in series. Packing fractures at the wall contribute a parallel admittance. Resistivity depends on both pore connectivity and the resistivity of the water [2]. We equilibrated the source material and the standards in the same cell bath and retained the four-terminal measurement geometry on all cylinders. Synthetic end membranes exposed to the bath gave an independent estimate of the electrode polarization. Their imaginary response was fitted over a frequency interval judged acceptable using residual phases in blank cells.

A radiograph of the filled cell gave an intact active-area fraction $1 - f = 0.9200$. The peripheral admittance per total area, $Y_{b} = 0.001200$ S/m², was obtained with the interior replaced by an insulating plug. If R is the resistance times active area, the observation law and local inversion are

$$Y = Y_{b} + \frac{1 - f}{R}, \qquad N_{\mathrm{core}} = \frac{1 - f}{a(Y - Y_{b})}. \tag{5}$$

The reference a is a thin bed reconstructed from sieved core grains. Its thickness equals the first integral correlation length, 2.50 mm, of the vertical packing fraction in the reference columns. The choice fixes a local interval over which representative-volume averages begin to stabilize [14, 24]. Resistance times area of one reconstructed bed was 0.25000 Ω m² from the slope of joint fits to its potential drop. Small gaps in cell inserts, which lengthen the electrical path along a wall, were measured with the plug in place. Two standards in series at matched contact pressure gave 0.498 Ω m². The bulk cylinder gave 0.0889653 S/m². After inversion on the intact area its resistance is 10.4825 Ω m², or 41.93 reference beds.

The shortest apparent path in the radiograph was in the annulus. Forcing it to carry the same current per area as the center yields 45.57 bed equivalents even if one keeps the independently measured bypass subtraction. No adjustment to the thickness of the reference bed can satisfy both that estimate and the series check at fixed contact pressure. The intact-area estimate proceeds from a measured geometric property of each cylinder.

4 Prediction at a fixed measurement boundary

The six central estimates appear in Figure 2 with the seventh shown separately at the right. With weights $w_j = u_j^{-2}$, the discovery fit is

$$\hat{\nu} = \frac{\sum_{j=1}^{6} w_j N_j}{\sum_{j=1}^{6} w_j} = 42.0151, \qquad u(\hat{\nu}) = \left(\sum_{j=1}^{6} w_j \right)^{-1/2} = 0.0812. \tag{6}$$

The residual sum of weighted squares is 1.04 on five degrees of freedom. The observed scatter is unusually small under independent Gaussian errors. Our standard uncertainties include type B contributions with poorly known sampling distributions, and some cover coherent motion across blocks that a between-system residual would be unlikely to exhibit in one realization. We retained the original uncertainties. Rescaling them to match the observed scatter would make the interval for the seventh system particularly difficult to interpret [6, 11].

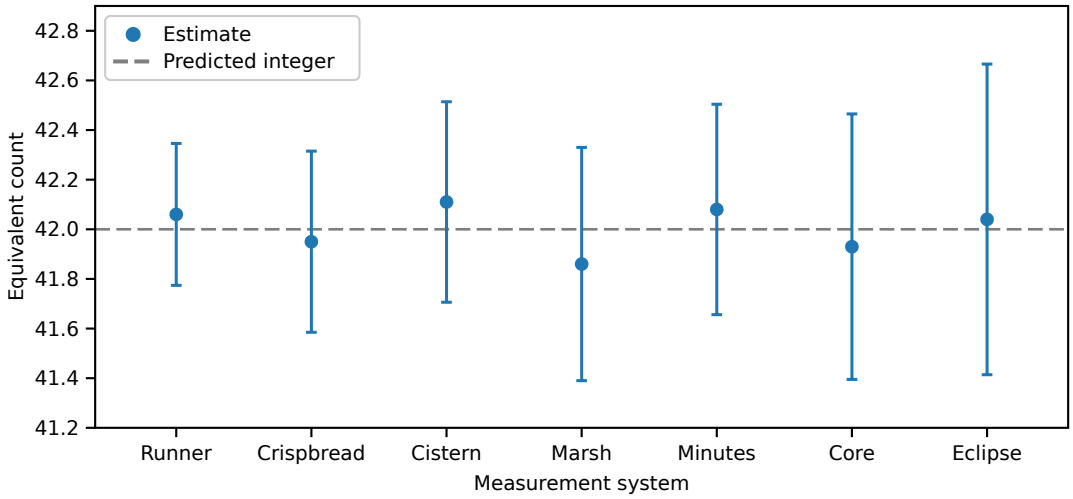


Figure 2: Equivalent counts and marginal 95% uncertainty intervals. The eclipse result is shown after unsealing. The horizontal reference is the integer selected from the first six systems.

The prediction registered for the seventh system was the integer nearest to Eq. (6). The record also included the local calibration and integration boundary. The eclipse interval was feasible at all four infrared bands and was fixed at the first 1,200 s of complete umbral coverage of the mapped patch. The count prediction evaluates the observation law at that boundary. Predicting a duration from the result would amount to selecting the integration boundary after looking at the heat release.

4.1 Radiative loss from the eclipsed surface

The lunar observation used a tracked patch of low-relief highland terrain and a fixed emission-angle mask. Four atmospheric-window bands were reduced to one surface temperature per pixel and sampling time, using measured band transmission and a temperature-independent emissivity spectrum. Thermal gradients in the upper regolith concern the conversion from duration to temperature [9]. Surface calorimetry only needs the outgoing flux and the absorbed external illumination at the same surface. We used a prior for the spectral emissivity from the companion pre-eclipse observations. The band entering deepest into the wing of the atmospheric water feature was fit with a separate offset constrained by the comparison sky track [15].

Let $T_i(t)$ denote the reconstructed surface temperature of footprint element i, w_i its horizontal area fraction in the common mask, ϵ_i its effective hemispheric emissivity, and $S(t)$ the absorbed external flux. For a surface with negligible storage in the optical skin, the integrated energy leaving the substrate through the surface is

$$Q = \int_{0}^{1200\,\mathrm{s}} \left[\sum_{i} w_i \epsilon_i \sigma T_i(t)^4 - S(t) \right] dt, \qquad N_{\mathrm{lun}} = Q / a_{\mathrm{lun}}. \tag{7}$$

The Planck inversion takes place before averaging over footprint area. Averaging temperature first gives a systematically smaller flux if emissivity is uniform. The absorbed illumination includes a correction for faint light in the umbra and for Earth emission at long wavelengths. The median correction is 0.13 W/m². Its sign lowers the estimate of heat released by the substrate. A small set of exposed rocks in the common mask contributes flux but is represented at its own temperature. An extrapolation of the median regolith temperature to those footprints would remove a high-temperature component identifiable in the joint fit.

The unit standard is the heat released in a ten-kelvin cooling span by a horizontal grain bed with thickness equal to its measured volume-weighted mean grain diameter. The cooling span was the operating interval of the laboratory differential calorimeter. A column of anorthositic particulate simulant of known footprint and areal mass was cycled over that interval centered on 180 K. Multiplying its mass-specific integrated heat capacity by the areal mass of one bed gives 1.3800 kJ/m². The corresponding values of the areal mass and mean heat capacity were 0.2760 kg/m² and 500.0 J/(kg K). This calculation transfers a heat standard, so the absolute grain diameter of the simulant enters through the measured areal mass of the laboratory bed. The lunar specimen’s depth does not enter Eq. (7). For comparison, applying the procedure to two standard beds with the same exposed area and initial temperature recovers twice the heat capacity within the calorimeter calibration.

Equation Eq. (7) then predicts $42 \times 1.3800 = 57.9600$ kJ/m². The six consecutive 200 s mean net fluxes in Figure 3 sum to an integral of 58.0152 kJ/m². The residual is +0.0552 kJ/m², or +0.04 on the equivalent-count scale. The uncertainty of the contrast, including standard, is about 0.44 kJ/m². The beginning of the thermal sequence has a steep temperature gradient in time.

When the analysis mistakenly included the last partial-illumination frame before the common mask was completely dark, the integrated value increased by 0.31 kJ/m². At the native sample cadence that increase was large enough to identify the affected bin by inspection of the residual flux. We used fractional exposure timing from the tracking record at the mask boundary.

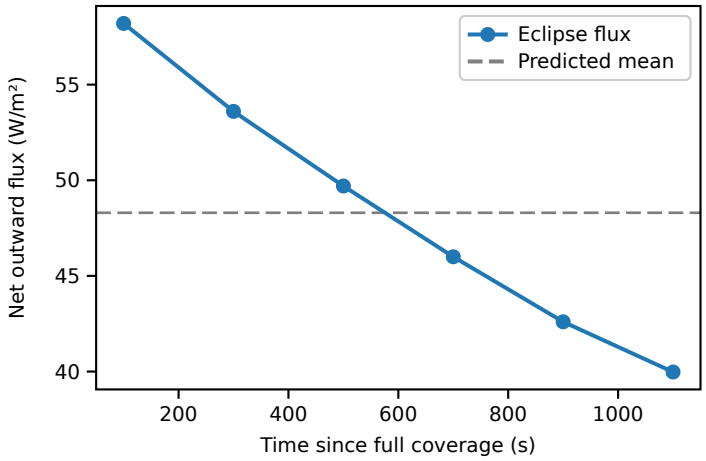


Figure 3: Mean net outward flux in consecutive 200 s bins within the held-out 1,200 s interval. Bin centers are shown. The horizontal line is the mean flux implied by the integer prediction and the laboratory areal heat standard.

A fit of the original six linear or transformed responses at the estimated value in Eq. (6) gives a forecast of 57.981 kJ/m² at the same boundary. The integer declaration sharpened the forecast by 0.021 kJ/m² in the downward direction. That difference is smaller than the uncertainty from the transfer standard. The point of specifying an integer forecast was to fix the convention ahead of the observation. Future observations would have to resolve the variation within the decimal range to establish whether the population value is exactly integral.

5 Uncertainty and robustness

We propagated reading noise by block, calibration uncertainty by standard, and acquisition-model uncertainty by varying the fitted response coefficients through the auxiliary likelihood. These components appear in Table 2 after projection to equivalent counts. Combining them is the local form of the law of propagation of uncertainty [11]. For the archive, both the release and inherited counts are taken from one packet. We kept their covariance inside the reading component. The gamma-shape and exposure estimates have a joint calibration covariance, likewise kept within one component. For lunar totality the spatial and time-block residuals describe reading uncertainty conditional on the single episode. The sample size of one eclipse cannot estimate variation between eclipses.

Table 2: Error budget in equivalent-count units. The last column is the quadrature total of the preceding columns. Within a column the design-level covariance is included before taking the square root.

System	Reading	Standard	Observation model	Combined u
Drawer runner	0.10	0.08	0.07	0.146
Crispbread sheet	0.12	0.11	0.09	0.186
Cistern decay	0.15	0.10	0.10	0.206
Marsh pollen	0.18	0.13	0.09	0.240
Minutes archive	0.15	0.12	0.10	0.217
Riverbed core	0.14	0.18	0.15	0.273
Lunar totality	0.16	0.21	0.18	0.320

Each interval $N_j \pm 2.69 u_j$ contains 42 and no other integer. Here 2.69 is a rounded-up normal quantile for simultaneous two-sided coverage of at least 95% by Bonferroni's inequality under the marginal Gaussian approximation. This statement does not depend on cross-system independence. It does depend on treating the error budget as uncertainty about a response at the specified protocol, including its composition model. The endpoints range from 41.18 to 42.90 across the seven systems. For comparison, rounding just the marginal means would give the same answer even if the combined uncertainty of every system were ten times as large.

Sensitivity runs fixed the standards or replaced them with an independent measurement of the same physical unit. We first dropped the latest block in acquisition order from each repeatable instrument. For the eclipse we suppressed the last block of frames when fitting the sky offset and evaluated the entire interval using that fit. Then we recovered the responses with the alternative observation model specified in Table 3. A two-unit reference divided by two in the additive coordinate was available for each case, either through a separately observed two-unit specimen or through a joint tracer exposure. Each case was re-estimated from the measured pair response. Composition of two acoustic coupons, for instance, uses half their joint log decrement. Halving their arithmetic energy fraction would give a unit fraction smaller by nearly a factor of two.

Table 3: Changes in the equivalent count relative to the primary protocol. The alternative recovery uses the same target observable and the same unit definition.

System	Terminal block omitted from fit	Alternative recovery	Measured pair as standard
Drawer runner	+0.04	Deflection hinge fit, +0.09	+0.07
Crispbread sheet	−0.05	Perimeter correction, +0.12	−0.08
Cistern decay	+0.07	All-bin log slope, −0.19	+0.11
Marsh pollen	−0.08	Short tracer windows, −0.12	−0.10
Minutes archive	+0.08	Docket-specific yields, −0.16	+0.15
Riverbed core	−0.06	Two-frequency cell fit, +0.17	+0.17
Lunar totality	+0.09	Three-band temperature fit, +0.14	−0.13

The sensitivity surface in Figure 4 shows the departure from 42 after each change. The largest excursion is -0.26 for the two-window pollen fit. The admissible alternatives use the same unit and still place all seven estimates closer to 42 than to any other integer. The exposure-averaging approximation in Section 3 for pollen and the forced-current approximation for sediment were excluded by their calibration experiments. They remain informative as controls on the scale of the changes caused by using the wrong observation law.

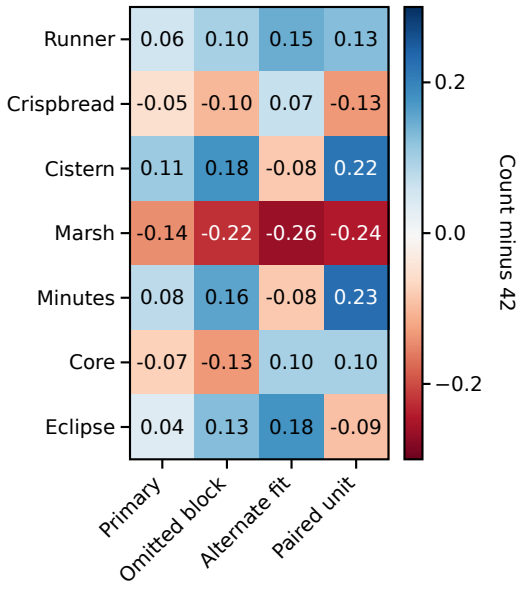


Figure 4: Estimate minus 42 for each sensitivity run. The display is centered on zero in equivalent-count units.

Leaving out one discovery system at a time gives pooled values from 41.995 to 42.035. The runner carries about 31% of the total discovery weight. Because it supplied the earliest candidate for the integer, we repeated the prediction after omitting it. The preferred integer for the eclipse remained 42 and the unrounded discovery mean decreased to about 41.995. Two-point observation combinations give a more sensitive check for calibration shift. For the marsh and the sediment, moving the standard by two standard uncertainties in the direction that lowers both counts gives respective estimates of 41.60 and 41.57. Their average is still on the same side of 41.5, with considerably less margin than in the primary analysis.

6 Scope of the correspondence

There is an empirical claim beyond Proposition 1. Within a specified acquisition boundary, changing the units of the observations or replacing a one-unit estimate by the per-unit response of an independently measured pair should leave the inferred count within calibration uncertainty. Once those checks pass, the rule used for the eclipse says that a unit standard alone predicts the magnitude of a yet-unseen specimen response. The lunar measurement is the only prospective test in the present series. The discovery cases were selected from instruments that passed their ordinary service checks and were practical to transfer. That selection was not random over possible physical or administrative systems. A chance calculation under a uniform distribution over integers would require a reference class of such systems. We have no sampling frame for that class.

Specimen boundaries are also consequential. Moving the front face used for the runner changes the predicted index count by the displacement between faces divided by the pitch. The eclipse prediction describes a specific surface footprint and time window. Integrating twice as long will generally yield less than twice the energy because the surface continues to cool. The canonical count of the longer interval is the sum of counts for its two successive parts. It is the same constant only if the full interval releases the same heat, which would require the added part to contribute zero. A test of invariance should specify which changes leave the observation boundary intact.

A direct use of the correspondence is a paired blind comparison. One group measures the energy of another registered eclipse footprint and another measures the retention of a production sheet from a separate bakery. Each group reports its own unit response and combined uncertainty before the two specimen values are released. At the precision of the present study one would expect both to resolve 42 if the same correspondence holds. For an experiment aimed at resolving a departure of one tenth of a unit, the lunar calorimeter and the sheet mass would both require improved standards. More observations at the current external-calibration precision would mainly refine the random part of the error.

A Scalar calculations and checks

For an additive measurement $N = y/a$, the components associated with independent y and a are u_y/a and $|N| u_a/a$. The acoustic derivatives at fixed geometry follow from Eq. (2). In particular,

$$\frac{\partial N_{\mathrm{cis}}}{\partial P} = \frac{1}{P \log a}, \qquad \frac{\partial N_{\mathrm{cis}}}{\partial a} = -\frac{N_{\mathrm{cis}}}{a \log a}. \tag{8}$$

The sensitivity to the calibration fraction increases near one. At fixed decay, increasing the reflected fraction per encounter increases the recovered encounter count.

For Eq. (3) we used $\theta_{\mathrm{eff}} = 3\theta_{\mathrm{gate}}$. The illustrative no-mixture count in Section 3 can be obtained from $\lim_{k\to\infty} k(P_0^{-1/k} - 1)/\theta_{\mathrm{eff}}$. The derivative in P_0 at constant k is $-P_0^{-1/k-1}/\theta_{\mathrm{eff}}$. It weights a given error in a low empty fraction more strongly. Window resampling was therefore done on exposures and the ratio recomputed after resampling, rather than resampling estimated counts from individual cells.

For the archive the adjustment subtracts $0.46(27.4) = 12.604$ inherited marks, leaving 23.64896. For the core it subtracts 0.001200 S/m² before division into the active fraction. Ordering those operations matters even when the annulus is small. At fixed f the local slope in Y is $-N/(Y - Y_b)$, so the signs of the bypass and bulk-admittance perturbations oppose one another. Uncertainty in the plug correction was treated as shared across the cylinders, as in the general case of a measured common blank [22].

The effective energy attributed to the lunar patch is calculated per horizontal projected area. The surface integrand is the sum over individual pixels corrupted by common radiometer gain and sky uncertainty. To linear order, a common temperature perturbation δT changes the net flux integrand by $4\sigma \delta T \sum_i w_i \epsilon_i T_i^3$. Averaging independent footprints does little to reduce this contribution. The six bin means in Figure 3, each with width 200 s, reproduce the integrated energy at the displayed precision.

Acknowledgments

We thank Noémia Sobreiro for reconciling the transfer-standard records and Irina Harvel for retaining the eclipse timestamp corrections with the mask files.

References

[1] János Aczél. *Lectures on Functional Equations and Their Applications*. Academic Press, 1966.

[2] G. E. Archie. The Electrical Resistivity Log as an Aid in Determining Some Reservoir Characteristics. *Transactions of the AIME*, 146:54–62, 1942. doi: 10.2118/942054-G.

[3] Martin I. Bezdan. Octave-Band Reflection of Mineral Coupons at Diffuse Incidence. Technical Report AC-22-04, Marven Institute, 2022.

[4] Percy W. Bridgman. *Dimensional Analysis*. Yale University Press, 1922.

[5] Edgar Buckingham. On Physically Similar Systems: Illustrations of the Use of Dimensional Equations. *Physical Review*, 4:345–376, 1914. doi: 10.1103/PhysRev.4.345.

[6] William G. Cochran. The Combination of Estimates from Different Experiments. *Biometrics*, 10:101–129, 1954. doi: 10.2307/3001666.

[7] William Feller. *An Introduction to Probability Theory and Its Applications*. Wiley, 1968.

[8] Simone Garveil and Luís M. Taveiro. Transfer of Displacement and Mass Standards Between the Cerdeiro and Marven Laboratories. Technical Report MT-19-07, Marven Institute, 2019.

[9] P. O. Hayne, J. L. Bandfield, M. A. Siegler, A. R. Vasavada, R. R. Ghent, J.-P. Williams, B. T. Greenhagen, O. Aharonson, C. M. Elder, P. G. Lucey, and D. A. Paige. Global Regolith Thermophysical Properties of the Moon From the Diviner Lunar Radiometer Experiment. *Journal of Geophysical Research: Planets*, 122:2371–2400, 2017. doi: 10.1002/2017JE005387.

[10] Philip Hougaard. Life Table Methods for Heterogeneous Populations: Distributions Describing the Heterogeneity. *Biometrika*, 71:75–83, 1984. doi: 10.1093/biomet/71.1.75.

[11] Joint Committee for Guides in Metrology. Evaluation of Measurement Data: Guide to the Expression of Uncertainty in Measurement. Technical Report JCGM 100:2008, Joint Committee for Guides in Metrology, 2008.

[12] Eva Linarev and Leonor M. Sobreiro. Repeatability of the Drained-Mass Assay for Baked Cereal Sheets. Technical Report VC-21-03, Instituto do Vale Cerdeiro, 2021.

[13] Darryl I. MacKenzie, James D. Nichols, Gideon B. Lachman, Sam Droege, J. Andrew Royle, and Catherine A. Langtimm. Estimating Site Occupancy Rates When Detection Probabilities Are Less Than One. *Ecology*, 83:2248–2255, 2002.

[14] Georges Matheron. Principles of Geostatistics. *Economic Geology*, 58:1246–1266, 1963. doi: 10.2113/gsecongeo.58.8.1246.

[15] Ilze Mevrani and Eun-seo Ryun. Photometric Offsets During Tracking of a Resolved Eclipsed Surface. Technical Report PR-24-11, Saeum Institute of Science, 2024.

[16] Salwa Ravehdi. Carry-Through Rates of Coded Annex References in Municipal Minutes. Technical Report AR-23-06, El Manarif School of Public Studies, 2023.

[17] J. Andrew Royle. N-Mixture Models for Estimating Population Size from Spatially Replicated Counts. *Biometrics*, 60:108–115, 2004. doi: 10.1111/j.0006-341X.2004.00142.x.

[18] Wallace Clement Sabine. *Collected Papers on Acoustics*. Harvard University Press, 1922.

[19] M. R. Schroeder. New Method of Measuring Reverberation Time. *Journal of the Acoustical Society of America*, 37:409–412, 1965. doi: 10.1121/1.1909343.

[20] Alena Stenavec. Displacement Standards for Loaded Index Stops. Technical Report MT-20-14, Marven Institute, 2020.

[21] S. S. Stevens. On the Theory of Scales of Measurement. *Science*, 103:677–680, 1946. doi: 10.1126/science.103.2684.677.

[22] John R. Taylor. *An Introduction to Error Analysis*. University Science Books, 1997.

[23] Nuria Valcero and Xavier Padril. Between-Gate Exposure Covariance in Marsh Pollen Collectors. Technical Report VC-21-19, Instituto do Vale Cerdeiro, 2021.

[24] Matteo Varolin and Cidália Avel. Vertical Packing Correlations in Reconstituted Estuarine Cores. Technical Report VC-22-08, Instituto do Vale Cerdeiro, 2022.

[25] Edward W. Washburn. The Dynamics of Capillary Flow. *Physical Review*, 17:273–283, 1921. doi: 10.1103/PhysRev.17.273.